The local intrinsic curvature of wavefronts allows to detect optical vortices

B. PAROLI,[*] M. SIANO, AND M. A. C. POTENZA

Dipartimento di Fisica, Universitá degli Studi di Milano, via G. Celoria, 16, 20133 Milano, Italy
[*]*bruno.paroli@unimi.it*

Abstract: We describe a method for effectively distinguishing the radiation endowed with optical angular momentum, also known as optical vortex, from ordinary light. We show that by detecting the inversion of the transverse intrinsic curvature sign (ITICS) an optical vortex can be locally recognized. The method is effective under conditions of huge importance for the exploitation of optical vortices, such as the far field of the source and access to a small fraction of the wavefront only. The validity of the method has been verified with table-top experiments with visible light, and the results show that a measurement performed over a transverse distance smaller than 4% of the beam diameter distinguishes a vortex from a Gaussian beam with a significance of 93.4%. New perspectives are considered for the characterization of vortices, with potential impact on the detection of extra-terrestrial radiation as well as on broadcast communication techniques.

1.   Introduction

Radiation carrying orbital angular momentum (OAM, or vortex) is a form of exotic radiation discovered at the end of the twentieth century as described by Allen et al. [1]. It differs from "ordinary" light since the quantized orbital angular momentum $L_z = l\hbar$ per photon, where l is an integer. This introduces an additional degree of freedom that opens new perspectives in different fields of applied and fundamental science such as singular and quantum optics [2, 3], astronomy and astrophysics [4–7], quantum information and computing [8, 9] as well as telecommunications [10–12].

From a classical point of view, the radiation wavefront of a vortex is an helicoid with winding number l. It is characterized by a phase singularity with zero intensity and by an azimuthal phase dependence $e^{i\phi(\theta)}$ of the associated scalar field around the singularity. The integral $l = \frac{1}{2\pi} \oint_{\Gamma} \nabla\phi \cdot \vec{ds}$ is the topological charge of the vortex, where Γ is a closed curve around the singularity.

Vortices can be easily produced in the laboratory by exploiting refractive optics or holographic methods. By contrast, a dowel is today missing concerning the existence of vortices from natural sources, including the case of extra-terrestrial sources. A possible reason for this comes from the relative difficulty in detecting and characterizing a vortex far from the source. Moreover, deep propagation of vortices has not yet been explored at any wavelength. To our knowledge, the maximum experimental distance covered by a vortex in free propagation is in the kilometric range, as for example achieved by Tamburini et al. [13] in 2012 and Krenn et al. [14] in 2014. Finally, up to now no experiment out of laboratory exists to clarify whether and how topological properties of vortices degrade through the Earth's atmosphere, nor the interstellar medium.

Several methods have been proposed in the past to measure vortex properties in the laboratory by using interference, diffraction [15–20] and refraction [21–23]. These techniques are generally intended to provide topological and phase properties by accessing a substantial portion of the vortex field around the phase singularity. An effective sorter of orbital angular momentum states has been proposed by Berkout et al. [24]. They converted the helically phased light beam into a beam with a transverse phase gradient by using two optical elements, illuminated by the entire
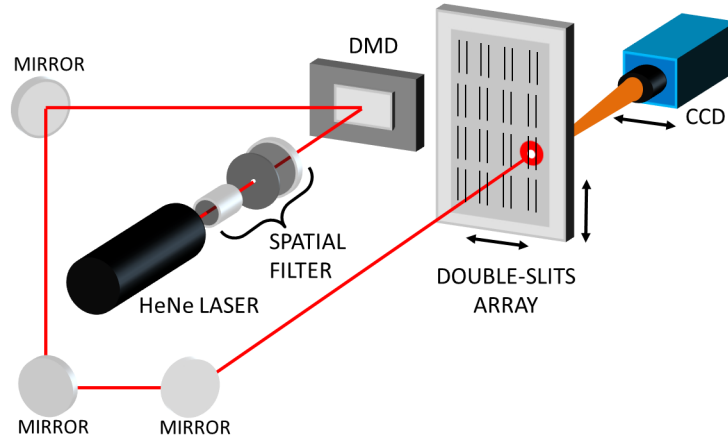
Fig. 1. Schematic representation of the experimental setup. Vortices are generated by diffraction from a holographic pattern imposed through a digital micromirror device (DMD). Intrinsic curvature is measured with the scanning interferometric technique detailed in [25] which uses an array of double-slits and a Charge Coupled Device (CCD) to perform measurements along linear profiles.

cross section of the incident beams.

In this work we propose and experimentally demonstrate an effective approach to measure vortices by accessing a small portion of the wavefront only. The method is based on the detection of the Inversion of the Transverse Intrinsic Curvature Sign (ITICS). Since the intrinsic curvature is a local differential property of the wavefront, this approach can really be strictly local, being ultimately related to the topological properties of the helicoidal surface.

To our knowledge this is the first experimentally proven method to recognize a vortex in a strictly local manner which is of utmost importance for working at large distances from the source, a definite need in many cases of interest.

2. Invertion of the transverse intrinsic curvature sign (ITICS)

Helicoidal wavefronts are ultimately different from ordinary light beams. By describing a wavefront as a differentiable regular surface, we introduce the first fundamental form $E du^2 + 2F du dv + G dv^2$ and second fundamental form $e(du)^2 + 2f du dv + g(dv^2)$, where E, F, G, e, f, g are 2-dimensional real functions defined for each point (u, v) of the surface. They are related to the intrinsic Gaussian and mean curvatures as $K_h = \frac{eg - f^2}{EG - F^2}$ and $H_h = \frac{eG - 2fF + gE}{2(EG - F^2)}$, respectively. In the case of an helicoid $E = 1$, $e = g = F = 0$, $G = c_h^2 + \rho_h^2$, $f = -c_h/\sqrt{c_h^2 + \rho_h^2}$. Therefore $K_h = -c_h^2/(c_h^2 + \rho_h^2)^2 < 0$ and $H_h = 0$, where ρ_h is the radial coordinate, $c_h = 1/k$ is the helicoid slant and k is the wavenumber.

We base our method on a fundamental property of helicoids that is to be minimal surfaces, $H_h = 0$. Thus the principal curvatures, deduced by K_h and H_h as $K_{1,2} = H_h \pm \sqrt{H_h^2 - K_h} = \pm c_h/(c_h^2 + \rho_h^2)$, have opposite signs at any point of the surface, $K_1 = -K_2$. This is not true for wavefronts of ordinary light (i.e. no minimal surfaces) in divergent free propagation which are generally characterized by principal curvatures of the same positive sign. Moreover, due to the conservation of the gaussian curvature under isometric transformations and because $K_h < 0$, the inversion of the curvature sign, $sign(K_1) = -sign(K_2)$, is a local intrinsic property of the
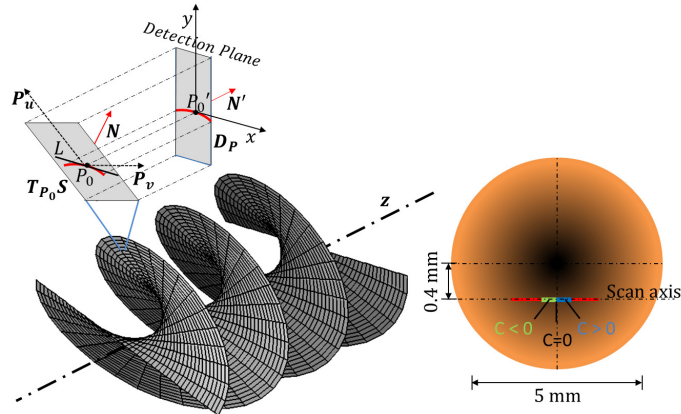
Fig. 2. Left: Sketch of the helicoidal wavefront of OAM radiation and projection of the normal curvature (red line) on the detection plane. The local frame is given by the independent vectors $(\mathbf{P_v}, \mathbf{P_u})$. On the detection plane the reference system has coordinates (x, y). Right: Representation of the scan path (red) across the vortex cross-section and the subintervals (green and blue) used for the local analysis.

curvature of OAM radiation. Therefore, we exploit the measurement of the ITICS to distinguish vortex radiation from ordinary light without any need to access the entire wavefront.

3. ITICS measurement with scanning interferometry

The technique we use to prove the ITICS is based on scanning interferometry of a double-slits array [26–31] however, other techniques able to measure the local curvature of the wavefront can be adopted to this aim, such as Hartmann-type wavefront sensors. The optical layout is schematically shown in Fig. 1. Two beams with charge $l = 1$ and $l = 0$, are generated from digital holograms produced by a DPL6500 Digital Micromirror Device (DMD) illuminated by a He-Ne spatially filtered laser beam. The beam impinges onto an array of double slits in order to measure the shear displacement Δp_ϕ as described in [25]. The method is realized by translating the double-slits along the horizontal axis in the detection plane with a step resolution of 40 μm. A cooled low-noise Charge Coupled Device (CCD) continuously tracks the slits in the observation plane at a distance of 45 cm from the detection plane and the interference pattern, produced at each scan step, is acquired for the analysis. The analysis occurs by selecting from the interference pattern a limited square region around each point of interest. The shear displacement is the horizontal distance between the central maximum of the interference pattern and the double slit center, measured in the limited region, as a function of the scan variable x. In the limit case of small scan step and slit separation, $\Delta x \to 0$, $D \to 0$ we write

$$\Delta p_\phi = \int \phi'' \frac{z'}{k} dx + K \tag{1}$$

where z' is the distance between the double-slit array and the detection plane, ϕ'' is the second derivative of the phase function ϕ, i.e. the radiation phase measured along the scanned profile, and K an additive constant. The shear displacement is easily related to the local curvature by means of

$$C = \frac{\phi''}{k} = \frac{1}{z'} \frac{d\Delta p_\phi}{dx}. \tag{2}$$

The detection plane is maintained perpendicular to the optical axis z and the scan is performed
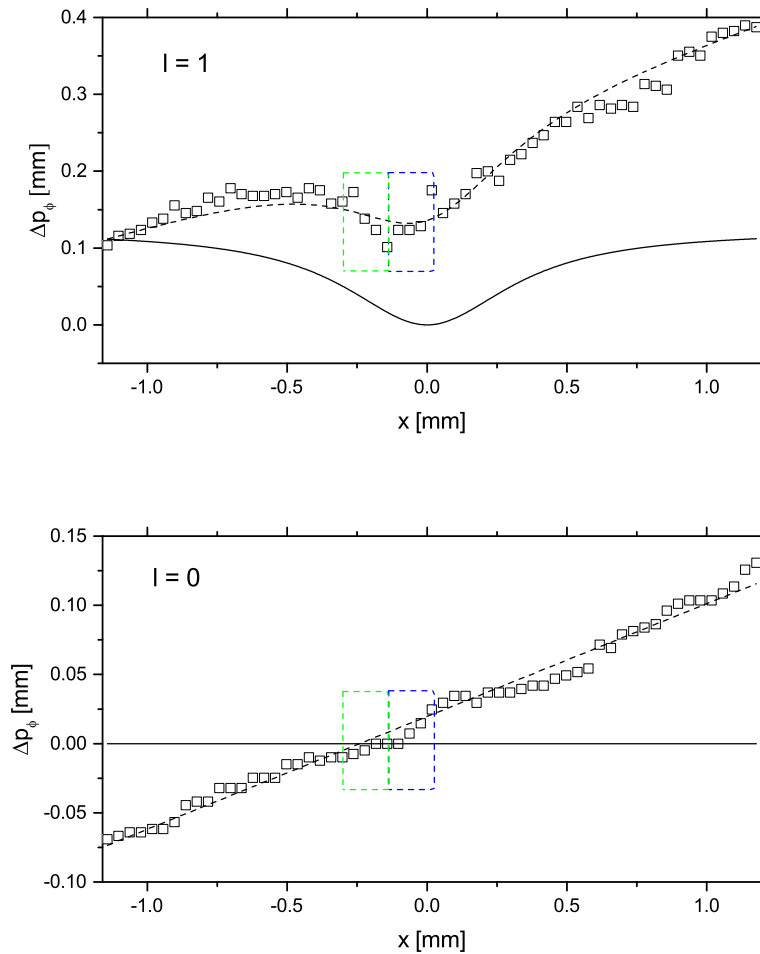
Fig. 3. Experimental data (squares) of the shear displacements Δp_ϕ of the $l = 1$ (top) and $l = 0$ (bottom) beams measured with horizontal scans across the extended region. Dashed lines are the best fits to data. Solid lines are the difference between the fitted lines and the linear drifts due to the beam divergence. The green and blue regions in the plots evidence data used in the local analysis. Notice that the magnitude of Δp_ϕ of $l = 1$ and $l = 0$ are not at the same level since the curvatures due to the beam divergence are different.
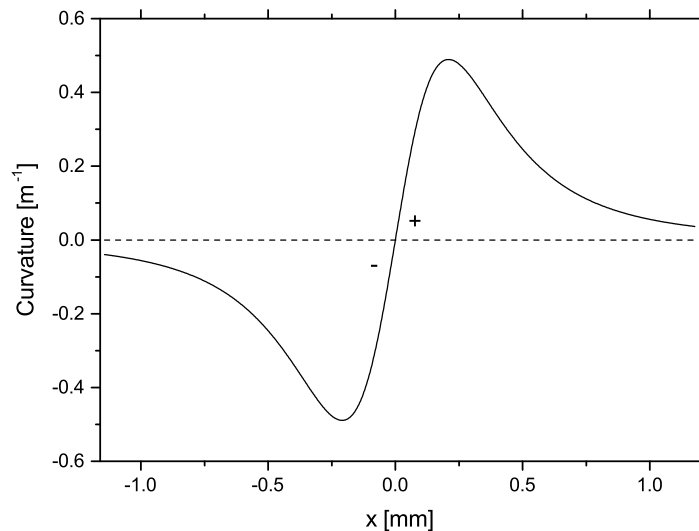
Fig. 4. Curvatures obtained from the fits shown in Fig. 3 for $l = 1$ and $l = 0$. The solid line is the difference between the curvature of the $l = 1$ beam and the curvature due to the beam divergence ($0.26\ m^{-1}$). The inversion of the beam curvature is evident at $x = 0$ mm. The dashed line is the difference between the curvature of the $l = 0$ beam and the curvature due to the beam divergence ($0.18\ m^{-1}$) which provides the curvature $C = 0$ of a collimated beam.

along a horizontal axis at a minimum distance of 0.4 mm below the singularity as shown in Fig. 2 (right). We first prove the correctness of the behavior of the shear displacement and the corresponding measuring method by reporting the results obtained by scanning a large region (2320 μm across, i.e. 46% of the beam diameter). Then we show that the analysis maintains its reliability by limiting the measurement to about 4% of the light beam diameter ($\pm$160 μm), thus providing the effectivness of the local measurement.

4. Extended measurement

The results are represented in terms of the shear displacement Δp_ϕ which is the quantity directly measured during the scan. The shear displacement in Eq. (10) has been derived theoretically in the appendix in order to fit the data and to check the consistency of the measurements with the theory. Equation (10) has been obtained considering the projections of the normal curvatures of the helicoid on the detection plane, as depicted in Fig. 2 (left). The projection gives a negligible relative discrepancy with respect to the curvature calculated in the tangent space $T_{P_0}S$ of the helicoid. The results of the extended measurement for a vortex ($l = 1$) and of a Gaussian beam ($l = 0$) are shown in Fig. 3. The reported shear displacements have been obtained by averaging the measurements from six scans with double slits 50 μm wide and spacing of 160 μm, 200 μm, 240 μm, 280 μm, 320 μm, 360 μm.

The divergence of the beam introduces a linear drift overlapped to the shear displacement caused by the intrinsic curvature of the helicoid. This effect is evident in both data and theory. In Fig. 3 the linear drifts have been subtracted from the theoretical fits (dashed lines) to obtain the shear displacements of collimated $l = 1$ and $l = 0$ beams (solid lines). The linear drift has been evaluated separately by fitting the shear displacement measured at $y = -2.7$ mm. Far from the
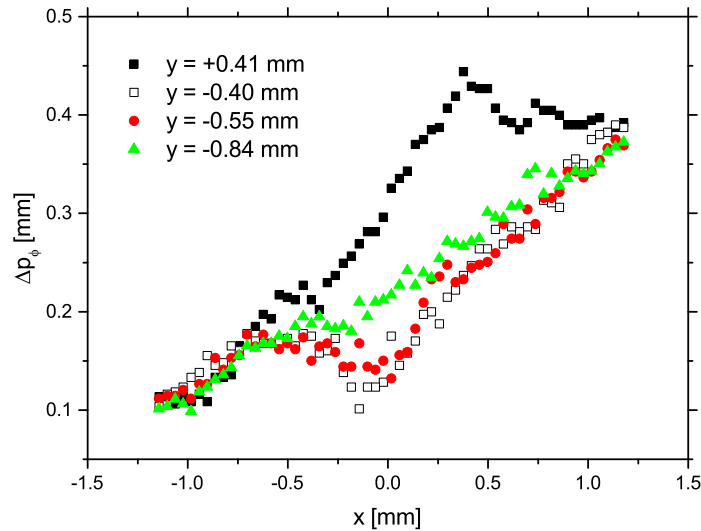
Fig. 5. Experimental data of the shear displacements Δp_ϕ of the $l = 1$ beam measured with horizontal scans across the extended region. The shear displacement has been evaluated at different vertical distances from the singularity.

singularity the variations of Δp_ϕ due to the intrinsic curvature are negligible with respect to the linear drift (due to the beam divergence) and r_d in Eq. (10) can be estimated more accurately.

The wavefront curvature across the sampled region has been estimated for both $l = 1$ and $l = 0$ from the shear displacements of Fig. 3 (solid lines) by using Eq. (2). Results are shown in Fig. 4 for both $l = 1$ and $l = 0$. The normal curvatures reverse their signs for $l = 1$ at $x = 0$ mm as shown by the solid line.

The method has been verified by performing the analysis at different distances from the singularity: $y = -0.55$ mm, $y = -0.84$ mm and $y = +0.41$ mm as shown in Fig. 5. By increasing the distance the peak of inversion becomes less visible since the Gaussian curvature of the helicoid decreases by increasing the radial coordinate, as predicted by Eq. (10). Furthermore, the shear displacement at $y = +0.41$ mm (solid black squares) shows a maximum instead of the minima observed for points with y<0. This is in agreement with the azimuthal symmetry of the helicoid.

When the scan direction is along the x axis the curvature changes from negative to positive in the negative half-plane $y < 0$, while it is reversed in the positive half-plane $y > 0$, the amplitude A in Eq. (10) is positive for $y > 0$ and negative for $y < 0$. Notice that the x position of the maximum is remarkably displaced on the right. A possible reason is a small misalignment (inclination) of the double-slit with respect to the y axis

5. Local measurement

The local measurement is a subinterval of the extended range obtained with the horizontal scan. It is strictly local since it corresponds to a limited scan range along the horizontal direction $-160 \leq x \leq 160 \, \mu$m. In the vertical direction the locality of the measurement is given by limiting the analysis of the interference pattern within the range $\pm 74 \, \mu$m (± 5 pixel) around the point of interest.
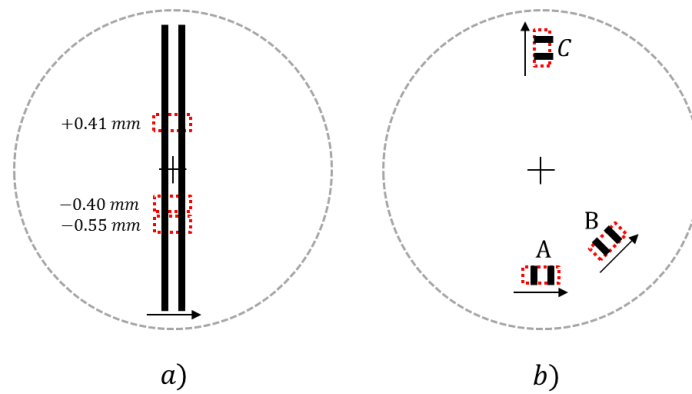
a) *b)*

Fig. 6. a) Representation of the spatial regions (red dashed lines) used in the experiment for the local analysis at different distances from the singularity. Each region has a horizontal range of ± 160 μm and vertical range ± 74 μm. b) Representation of other possible scan orientations. The ITICS is detected when the scan direction is orthogonal to the radial direction as in A and B. The scan along the radial direction as in C cannot be used to detect the ITICS.
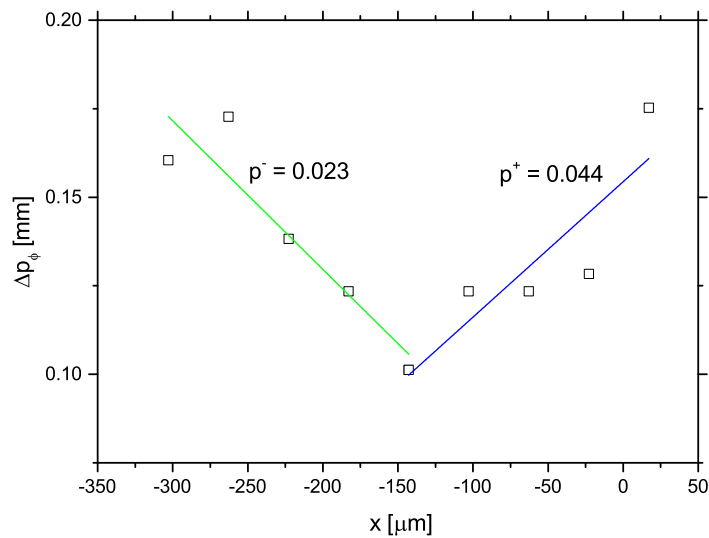

Fig. 7. Local analysis of the ITICS around $x = -143$ μm, $y = -0.40$ mm as in Fig. 3. $p^{\pm}$ are the probabilities that random fluctuations give correlation coefficients $|r| \geq |r^{\pm}|$.
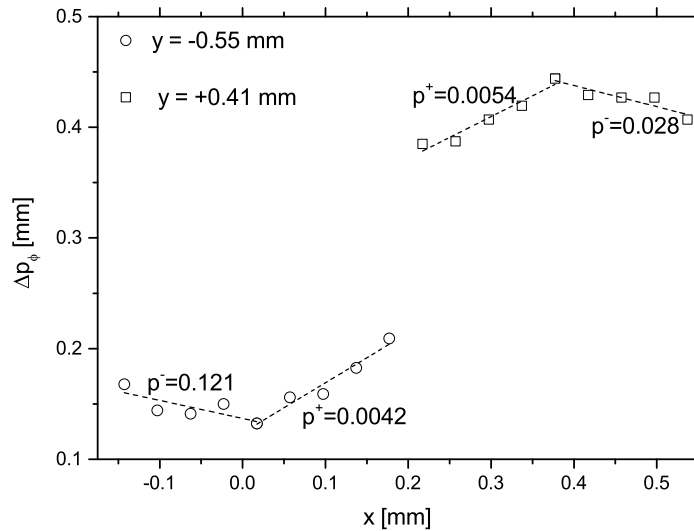
Fig. 8. Local analysis of the ITICS around the point at $y = -0.55$ mm and $y = 0.41$ mm as in Fig. 5. $p^{\pm}$ are the probabilities that random fluctuations give correlation coefficients $|r| \geq |r^{\pm}|$.

In Figure 6(a) we show the scan regions used in the experiment. The red dashed lines represent the regions of the local measurement around any point at different vertical distances from the singularity, while the black arrow shows the scan direction, always orthogonal to the radial direction.

In general, different conditions of detection could be adopted as shown in Fig. 6(b). The ITICS can be detected at any position (except the singularity), but it cannot be detected at any orientation. A convenient orientation is given by the orthogonality between the scan direction and the radial direction (see the points A and B in Fig. 6(b)) where the second derivative of the phase function and hence the curvature exhibits the change of sign. On the contrary, a scan along the radial direction, as in the case of the point C sketched in Fig. 6(b), does not produce any inversion, being constant the phase function (for the collimated beam). When the position of the singularity is unknown, several scans are necessary, until the orthogonality between the scan direction and the radial direction is obtained. Moreover the slit length can be certainty shorter than the vortex size, for example a double pinhole can be also used for measurements of the shear displacement.

We now prove the capability of ITICS to provide local measurements within the green and blue regions shown in Fig. 2 (right). Each region corresponds to less than 4% of the vortex ring diameter, defined as two times the distance between the maximum of intensity of the ring and the singularity. Notice that in the local analysis the divergence does not need to be separately determined from additional measurements. The ITICS is detectable from Δp_{ϕ} also with the linear drift due to the beam divergence. The linear fits of Δp_{ϕ} in the two regions are shown in Fig. 7. The probability that the inversion is not due to a random fluctuation is $[1 - p^{+}(|r| \geq |r^{+}|)][1 - p^{-}(|r| \geq |r^{-}|)] = 0.934$, where $r^{+} = 0.89$ and $r^{-} = -0.93$ are the correlation coefficients of the data from the green and blue regions respectively and

$$p^{\pm}(|r| \geq |r_0|) = \frac{2\Gamma[(n-1)/2]}{\sqrt{\pi}\Gamma[(n-2)/2]} \int_{|r_0|}^{1} (1 - r^2)^{(n-4)/4} dr, \tag{3}$$

where Γ is the gamma function and $n = 5$ is the number of points used to estimate $p^{\pm}$. Conversely, the local analysis of the $l = 0$ beam does not show any inversion in the region of interest since the correlation coefficients are both positive in the green ($r_g = 0.97$) and blue ($r_b = 0.96$) regions. Furthermore the probability that the missing inversion is due to random fluctuations is 1.4%. Local analysis has been performed for the points positioned at $y = -0.55$ mm and $y = +0.41$ mm and the results are shown in Fig. 8. The probabilities that the inversion is not due to random fluctuations are 87.5% and 96.7%, respectively. The lower probability at $y = -55$ mm is motivated by the lower visibility of the peak, which decreases the signal-to-noise-ratio.

6. Conclusions

Our choice for the scan extension is dictated by the instrumental apparatus, having 40 μm resolution and 10 μm measurement accuracy. By improving the instrumentation in resolution and accuracy, the scan extension can be in principle arbitrarily reduced. As an example, with a few micrometers in both resolution and accuracy the scan extension can be down to 0.4% of the entire wavefront.

We stress that in our measurements we compared two regions (green and blue in Fig. 2) just for practical reasons. Actually, the ITICS method can be adopted by performing measurements with different orientations around the same point (green or blue) by rotating the scan directions transversely to the propagation axis.

When the geometry is unknown, several scans with different orientations (transversely to the propagation axis) around the same point are necessary to detect the ITICS but with the huge advantage of being able to distinguish OAM radiation at any arbitary point of the wavefront.

In principle, false positives can be also detected with the proposed method, since helicoids are not the only known minimal surfaces, but other kinds of radiation wavefronts which are minimal surfaces (i.e. the ITICS occurs at any point of the wavefront) are today unknown, except the case of radiation carrying orbital angular momentum.

In conclusion, we have shown that by characterizing the ITICS an helicoidal wavefront can be recognized from a Gaussian beam in divergent free propagation. We prove that over a scan extension smaller than 4% of the beam diameter we can distinguish the vortex beam with a significance larger than 93%. This limit can be reduced by improving the resolution and accuracy of the measurements, thus making the method capable of a reliable local detection of a vortex over a very small fraction of the wavefront.

The combination of working in the far field of the source and the local character of the measurement opens the way to characterize vortices in a completely new set of conditions, from extra-terrestrial sources to signal transmission at large distances.

Appendix: derivation of the projected curvature and fit function

Let $T_{P_0}S$ be the tangent space of the helicoidal wavefront S at the point P_0 and the detection plane D_P orthogonal to the axis of propagation as sketched in Fig. 2.

Let's define the phase function $\phi(s)$ along a linear path L in $T_{P_0}S$ as the actual phase of the radiation field along the straight line L parametrized by s and passing through P_0 in $T_{P_0}S$.

Let's define the projection of the phase function $\phi(s)$ along z the new function

$$\phi_P(s) = \phi(s) + D(s)k, \tag{4}$$

where D is the distance of light propagation between P_0 and the corresponding projection P_0' in D_P. $\phi_P(s)$ is the phase observed in P_0' according to Fermat's Principle of light propagation in an

homogeneous medium.

We need the phase function ϕ_P to be described in the reference frame (x, y) rather than the local one. We then introduce the independent variable q defined in the frame (x, y) which is related to s by means of the linear transformation

$$s = \alpha q, \tag{5}$$

where α depends on the reciprocal orientation of the plane D_P with respect to $T_{P_0}S$. $\alpha = 1$ when D_P and $T_{P_0}S$ are parallel. As shown in [25] and in Eq. (2) the curvature of radiation along a linear path is locally given by the second derivative of the phase function. By using Eqs. (4) and (5) we have

$$\phi_P''(q) = \phi''(s)\left(\frac{ds}{dq}\right)^2 + kD''(s)\left(\frac{ds}{dq}\right)^2 . \tag{6}$$

Because the distance $D(s)$ is a linear application we obtain the projection as

$$\phi_P''(q) = \phi''(s)\alpha^2 \tag{7}$$

and hence

$$C = C_N \alpha^2, \tag{8}$$

where C_N is the curvature in P_0 along the direction of the linear path in the tangent space and C is the projected curvature measured in the detection plane described in the (x, y) frame. For an helicoidal wavefront with pitch $2\pi c_h \approx 633$ nm detected at a distance $\rho_h \approx 0.4$ mm from the singularity at the angle $\theta = -\pi/2$ (with respect to the horizontal axis) we obtain $\alpha^2 = cos^2(c_h/\rho_h)$. The relative discrepancy of C with respect to C_N is $1 - \alpha^2 \approx 6.3 \cdot 10^{-8}$ and can be neglected for our aims. The first derivative of the phase function $\phi'(q)$ of the helicoid along the horizontal axis in the detection plane is

$$\phi'(q) = \frac{\sqrt{1 - \frac{q^2}{q^2 + \rho_h^2}}}{\sqrt{q^2 + \rho_h^2}}. \tag{9}$$

Because $\Delta p_\phi \propto \phi'$ (see Eq. (1) and Eq. (2)) the theoretical function to fit the experimental data (as a function of the x coordinate) takes the form

$$\Delta p_\phi(x) = A\frac{\sqrt{1 - \frac{(x-x_0)^2}{(x-x_0)^2 + \rho_h^2}}}{\sqrt{(x-x_0)^2 + \rho_h^2}} + r_d x + K \tag{10}$$

where x_0, A, ρ_h, are the fit parameters, r_d is the shear ratio due to the beam divergence and finally K is an additive constant so that $min\{\Delta p_\phi(x) - r_d x\} = 0$.

References

1. L. Allen, M. W. Beijersbergen, R. J. C. Spreeuw, and J. P. Woerdman, "Orbital angular momentum of light and the transformation of Laguerre-Gaussian laser modes," Phys. Rev. A **45**, 8185–8189 (1992).
2. A. Mair, A. Vaziri, G. Weihs, and A. Zeilinger, "Entanglement of the orbital angular momentum states of photons," Nature **412**, 313–316 (2001).
3. M. Soskin, S. V. Boriskina, Y. Chong, M. R. Dennis, and A. Desyatnikov, "Singular optics and topological photonics," J. Opt. **19**, 010401 (2016).
4. F. Tamburini, G. Anzolin, G. Umbriaco, A. Bianchini, and C. Barbieri, "Overcoming the Rayleigh criterion limit with optical vortices," Phys. Rev. Lett. **97**, 163903 (2006).

5. G. Anzolin, F. Tamburini, A. Bianchini, G. Umbriaco, and C. Barbieri, "Optical vortices with star light," Astron. Astrophys. **488**, 1159–1165 (2008).
6. F. Tamburini, B. Thidé, G. Molina-Terriza, and G. Anzolin, "Twisting of light around rotating black holes," Nat. Phys. **7**, 195–197 (2011).
7. F. Tamburini, B. Thidé, and M. Della Valle, "Measurement of the spin of the M87 black hole from its observed twisted light," arXiv:1904.07923 [astro-ph.HE] (2019).
8. R. Inoue, T. Yonehara, Y. Miyamoto, M. Koashi, and M. Kozuma, "Measuring Qutrit-Qutrit entanglement of orbital angular momentum states of an atomic ensemble and a photon," Phys. Rev. Lett. **103**, 110503 (2009).
9. S. J. Tempone-Wiltshire, S. P. Johnstone, and K. Helmerson, "Optical vortex knots - one photon at a time," Sci. Rep. **6**, 24463 (2016).
10. Z. Wang, N. Zhang, and X.-C. Yuan, "High-volume optical vortex multiplexing and de-multiplexing for free-space optical communication," Opt. Express **19**, 482–492 (2011).
11. Y.Yan, G. Xie, M.P.J. Lavery, H. Huang, N. Ahmed, C. Bao, Y. Ren, Y. Cao, L. Li, Z. Zhao, A.F. Molisch, M. Tur, M.J. Padgett, and A.E. Willner, "High-capacity millimetre-wave communications with orbital angular momentum multiplexing," Nat. Commun. **5**, 4876 (2014).
12. C. Zhang and L. Ma, "Detecting the orbital angular momentum of electro-magnetic waves using virtual rotational antenna," Sci. Rep. **7**, 4585 (2017).
13. F. Tamburini, E. Mari, A. Sponselli, B. Thidé, A. Bianchini, and F. Romanato, "Encoding many channels on the same frequency through radio vorticity: first experimental test," New J. Phys. **14**, 033001 (2012).
14. M. Krenn, R. Fickler, M. Fink, J. Handsteiner, M. Malik, T. Scheidl, R. Ursin, and A. Zeilinger, "Communication with spatially modulated light through turbulent air across Vienna," New J. Phys. **16**, 113028 (2014).
15. J. Vickers, M. Burch, R. Vyas, and Surendra Singh, "Phase and interference properties of optical vortex beams," J. Opt. Soc. Am. A **25**, 823–827 (2008).
16. V. Carpentier, H. Michinel, and J. R. Salgueiro, "Making optical vortices with computer-generated holograms," Am. J. Phys. **76**, 916–921 (2008).
17. Y. Shen, G.T. Campbell, B. Hage, H. Zou, B.C. Buchler, and P.K. Lam, "Generation and interferometric analysis of high charge optical vortices," J. Opt. **15**, 044005 (2013).
18. H. Zhou, S. Yan, J. Dong, and X. Zhang, "Double metal subwavelength slit arrays interference to measure the orbital angular momentum and the polarization of light," Opt. Lett. **39**, 3173–3176 (2014).
19. J. Zhu, P. Zhang, D. Fu, D. Chen, R. Liu, Y. Zhou, H. Gao, and F. Li, "Probing the fractional topological charge of a vortex light beam by using dynamic angular double slits," Photon. Res. **4**, 187–190 (2016).
20. B. Paroli, A. Cirella, I. Drebot, V. Petrillo, M. Siano, and M. A. C. Potenza, "Asymmetric lateral coherence of OAM radiation reveals topological charge and local curvature," J. Opt. **20**, 075605 (2018).
21. M. P. J. Lavery, D. J. Robertson, G. C. G. Berkhout, G. D. Love, M. J. Padgett, and J. Courtial, "Refractive elements for the measurement of the orbital angular momentum of a single photon," Opt. Express **20**, 2110–2115 (2012).
22. M. Mirhosseini, M. Malik, Z. Shi, R.W. Boyd, "Efficient separation of the orbital angular momentum eigenstates of light," Nat. Commun. **4**, 2781 (2013).
23. C. Li and S. Zhao, "Efficient separating orbital angular momentum mode with radial varying phase," Opt. Express **5**, 267–270 (2017).
24. G.C.G. Berkhout, M.P.J. Lavery, J. Courtial, M.W. Beijersbergen, and M.J. Padgett, "Efficient sorting of orbital angular momentum states of light," Phys. Rev. Lett. **105**, 153601 (2010).
25. B. Paroli, M. Siano, and M. A. C. Potenza, "Asymmetric lateral coherence allows precise wavefront characterization," Europhys. Lett. **122**, 44001 (2018).
26. B. Paroli, E. Chiadroni, M. Ferrario, A. Mostacci, V. Petrillo, M.A.C. Potenza, A.R. Rossi, and L. Serafini, "Coherence properties and diagnostics of betatron radiation emitted by an externally-injected electron beam propagating in a plasma channel," Nucl. Instrum. Meth. Phys. Res. B **355**, 217–220 (2015).
27. B. Paroli, E. Chiadroni, M. Ferrario, V. Petrillo, M.A.C. Potenza, A.R. Rossi, L. Serafini, and V. Shpakov, "Asymmetric lateral coherence of betatron radiation emitted in laser-driven light sources," Europhys. Lett. **111**, 44003 (2015).
28. B. Paroli, E. Chiadroni, M. Ferrario, and M.A.C. Potenza, "Analogical optical modeling of the asymmetric lateral coherence of betatron radiation," Opt. Express **23**, 29912–29920 (2015).
29. B. Paroli, E. Bravin, S. Mazzoni, G. Trad, and M.A.C. Potenza, "A modified two-slit interferometer for characterizing the asymmetric lateral coherence of undulator radiation," Europhys. Lett. **115**, 14004 (2016).
30. B. Paroli and M.A.C. Potenza, "Two dimensional mapping of the asymmetric lateral coherence of thermal light," Opt. Express **24**, 25676–25683 (2016).
31. B. Paroli, E. Chiadroni, M. Ferrario, and M.A.C. Potenza, "A systematic study of the asymmetric lateral coherence of radiation emitted by ultra-relativistic particles in laser-driven accelerators," Nucl. Instrum. Meth. Phys. Res. A **839**, 1–5 (2016).